JGR Planets

Key Points:

- Emirates Mars Mission (EMM)-Emirates eXploration Imager (EXI) can capture full disk views of Mars at a time step of hours or less
- We created a dust storm database based on EMM-EXI images for Martian year 36 at the beginning of the EMM science phase
- Significant attention is given to characterizing the sub-diurnal variability of the storms, which is not previously emphasized

Supporting Information:

Supporting Information may be found in the online version of this article.

Correspondence to:

B. K. Guha,
bijayguha@uaeu.ac.ae

Author Contributions:

Conceptualization: Bijay Kumar Guha, Claus Gebhardt, Luca Montabone
Formal analysis: Bijay Kumar Guha, Claus Gebhardt, Roland M. B. Young, Luca Montabone
Funding acquisition: Claus Gebhardt, Roland M. B. Young
Investigation: Bijay Kumar Guha, Claus Gebhardt, Roland M. B. Young, Luca Montabone
Methodology: Bijay Kumar Guha, Michael J. Wolff, Luca Montabone
Project administration: Claus Gebhardt, Roland M. B. Young
Resources: Bijay Kumar Guha, Roland M. B. Young, Michael J. Wolff

Seasonal and Diurnal Variations of Dust Storms in Martian Year 36 Based on the EMM-EXI Database

Bijay Kumar Guha[1] , Claus Gebhardt[1,2] , Roland M. B. Young[1,2,3] , Michael J. Wolff[4] , and Luca Montabone[4,5,6]

[1]National Space Science & Technology Center, United Arab Emirates University, Al Ain, United Arab Emirates, [2]Department of Physics, College of Science, United Arab Emirates University, Al Ain, United Arab Emirates, [3]Department of Physics, SUPA, University of Aberdeen, King's College, Aberdeen, UK, [4]Space Science Institute, Boulder, CO, USA, [5]Laboratoire de Météorologie Dynamique, IPSL/CNRS/Sorbonne Université, Paris, France, [6]Paneureka, Le Bourget-du-Lac, France

Abstract The Emirates eXploration Imager (EXI) onboard the Emirates Mars Mission (EMM) is a dual-telescope camera system capable of observing various Martian atmospheric phenomena. The spacecraft's unique orbit allows the EXI to capture full disk views of Mars at a time step of hours or less, with a resolution of ∼2–4 km per pixel (in the nadir-looking direction) in both visible and UV channels. Leveraging these unparalleled observations, we conducted a comprehensive analysis of dust storms for Martian year (MY) 36, in alignment with EMM's scientific goals. This study involved the compilation of a dust storm database covering one MY using EMM-EXI images. This database contains essential information such as the start and end times of dust storms, their areal extent, and the latitude and longitude of the centroid. Furthermore, we devote significant attention to characterizing sub-diurnal variability, a facet not previously emphasized, by meticulously tracking dust storm evolution across multiple local times. Our analysis also delves into the origins, pathways, and morphological attributes of these dust storms. Overall, we catalog a total of 98 dust storms until the end of MY 36 (excluding the polar cap edge dust storms) since the beginning of the EMM science phase, and discuss their diurnal, seasonal, and spatial variability while comparing with some previously published findings. Additionally, we address the potential impact of EMM's coverage on the variability of these dust storms, drawing insights from a well-established multi-year database prepared from the observations of the Mars Color Imager onboard the Mars Reconnaissance Orbiter.

Plain Language Summary The Emirates Mars Mission (EMM) uses a camera called the Emirates eXploration Imager (EXI) to take pictures of Mars. The EMM spacecraft moves in a unique way that allows the EXI to take pictures of the whole planet multiple times a day. We used the EXI images to learn about dust storms during one Martian year. We created a database with information about when dust storms started and ended, how big they were, and where they occurred on the planet. We found 98 dust storms during this time and compared the findings with previously published results. We observed a strong influence of the atmospheric thermal tides on the occurrence of dust storms over different times of the day, with the peak phases for the large storms mostly between 10 and 16 hr. We observed four different clusters and two pauses in the distribution of dust storms between the southern and northern spring seasons. Finally, we assess the EMM coverage bias on the frequency of dust storms observed with the help of already-established findings from another Mars mission. Overall, this study helps us understand more about dust storms on Mars and how they behave over times of a day or seasons.

1. Introduction

Dust is ubiquitous in the Martian atmosphere, although it shows strong spatial and seasonal variability. Atmospheric dust can form structures such as dust storms or dust devils influenced by circulations at different spatial scales (Cantor et al., 2001; Spiga & Lewis, 2010). Boundary layer eddies lift and transport dust on a small spatial scale (a few meters to several kilometers), forming dust devils (DDs, Balme & Greeley, 2006; Thomas & Gierasch, 1985). Mesoscale circulations create large dusty fronts along polar cap edges or through slope winds, creating local to regional dust storms (Malin et al., 2008; Rafkin et al., 2002; Toigo et al., 2002). Simultaneous occurrence of regional storms sometimes encircles the globe, enhancing global dust transport and loading by several times than the typical seasonal mean, creating global or extremely large and intense dust storms (Gillespie

Software: Bijay Kumar Guha
Supervision: Bijay Kumar Guha, Claus Gebhardt, Michael J. Wolff
Validation: Bijay Kumar Guha, Michael J. Wolff
Visualization: Bijay Kumar Guha, Claus Gebhardt
Writing – original draft: Bijay Kumar Guha
Writing – review & editing: Bijay Kumar Guha, Claus Gebhardt, Roland M. B. Young, Michael J. Wolff, Luca Montabone

et al., 2020; Guha & Panda, 2021, 2022; Guzewich et al., 2019, 2020; Kass et al., 2019; Montabone et al., 2015, 2020; Wolkenberg et al., 2020; Zurek & Martin, 1993).

Dust, once lifted into the atmosphere, stays suspended for a long period, and plays a pivotal role in enhancing the circulation strength by the radiative forcing, which modifies the regional/global weather and climate (Forget et al., 1999; Gebhardt et al., 2021; Guha & Panda, 2022; Guha et al., 2019; Haberle et al., 1982; Kahre et al., 2005; Liu et al., 2003; T. Z. Martin & Kieffer, 1979; Newman et al., 2002; Smith et al., 2001; Wilson, 1997; Zurek & Martin, 1993). The radiative impact of the dust on the atmosphere has a strong diurnal variation (Haberle et al., 1982; Lee et al., 2009; Madeleine et al., 2012; Medvedev et al., 2011; Smith et al., 2001; Zurek et al., 1992). Additionally, the dust particles, as ice condensation nuclei, subsequently impact the radiation budget and control the water transport between hemispheres (Clancy et al., 1996; Montmessin et al., 2004). The impact of dust storms includes but is not limited to thermal tides (Kass et al., 2019; Viúdez-Moreiras et al., 2019), polar ice caps (through dust deposition or mantling onto the caps) and albedo, hygropause altitude (by enhancing the saturation vapor pressure) (Kass et al., 2019; Piqueux et al., 2015; Viúdez-Moreiras et al., 2019), and photochemical loss rate and escape processes (through expansion of the upper atmosphere) (Aoki et al., 2019; Fang et al., 2020). Hence, a better understanding of dust storm variability is necessary to understand Martian weather and climatic processes.

Observational data sets from different Mars missions represent a key component available for studying the seasonal and climatic behavior of dust storms. This wealth of continuous satellite observation is available for a period of more than two decades for conducting Mars-specific scientific research. Several studies utilized imaging observations or direct aerosol measurements to understand the morphology and dynamics of dust storms during past decades (e.g., M. Battalio & Wang, 2019; Cantor, 2007; Gebhardt et al., 2023; Guha & Panda, 2021; Guha et al., 2019; Heavens et al., 2018; Kass et al., 2016; L. J. Martin & Zurek, 1993; Wang & Ingersoll, 2002; Wang & Richardson, 2015). Most of these studies rely on the data sets from sun-synchronous polar orbiters, which is great for studying the day-to-day or seasonal changes related to any atmospheric feature, such as dust storms. However, this viewing geometry has limited diurnal coverage. This gap can be reduced significantly using the observations from the Emirates Mars Mission (EMM), which offers global geographic and local time coverage on a timescale of 9–10 days. This scale corresponds to ∼5° of solar longitude (L_s) and ∼4 orbits of the spacecraft (Almatroushi et al., 2021).

In this paper, we use imaging data from EMM- Emirates Exploration Imager (EXI) to map and monitor the evolution of dust storms during Martian year (MY) 36. Here, we focus on characterizing the dust storms at a sub-daily time scale by tracking their evolution at multiple local times per day. This sub-daily scale variation considering a large latitude range has not been emphasized before. We describe the data set and methods used in this study for the detection of dust storms in Section 2. Section 3 describes the comprehensive dust storm database prepared from the images. Then, Section 4 presents the findings from the database related to the seasonal and diurnal variations of the dust storms. In Section 5, we tried to assess the bias from EMM coverage on the dust storm observations. Finally, Section 6 summarizes the results of this study.

2. Data and Methodology

The EMM "Hope (Al Amal)" probe was developed by the United Arab Emirates (Almatroushi et al., 2021; Amiri et al., 2022), and is the first Mars mission led by an Arab country. The science phase of EMM officially began in May 2021 (equivalent to L_s 49° of MY 36), which is the beginning of our study period. EMM has a unique science orbit, with altitudes varying between 20,000 km and 43,000 km, a near-equatorial inclination of 25°, and an orbital period of ∼55 hr. This orbit allows us to see Mars at a broad range of local solar times along with the seasonal coverage. The EXI onboard EMM operates in six spectral bands (Jones et al., 2021). The three visible (VIS) bands and three ultraviolet (UV) bands are centered near the wavelengths 635, 546, 437, 320, 260, and 220 nm, respectively. The pixel size in the nadir-looking direction varies between 2 and 4 km from the periapsis to the apoapsis of the EMM orbit, and the pixel footprint increases by a factor of [1/cos(e)] for the off-nadir looking direction. Here, e is the Emission angle.

In this study, we have used the level 2A images from the EXI observation modes XOS1, XOS4 and XOS6. Level 2A is the calibrated image, including metadata such as latitude and longitude. The XOS1 data product employs spatial binning of 2×2 pixels for 635 nm and UV images and 4×4 pixels for the 546 and 437 nm images. As a result, the pixel size increased by a factor of 2 and 4, respectively. XOS1 is a routine observation mode that takes

images every ∼2–3 hr. XOS4 takes full-resolution visible and 2 × 2 binned UV images, taken roughly once per week. XOS6, on the other hand, is a specialized "high-cadence" observation mode that takes sequences of images with a sub-hour time step. XOS6 data product uses the spatial binning of 2 × 2 pixels for all the VIS and UV bands. The EXI level 2A images are archived at the EMM Science Data Center (https://sdc.emiratesmarsmission.ae/). We also used the Mars Dust Activity Database (MDAD; M. Battalio & Wang, 2021) and the Mars Climate Database (MCD; Forget et al., 1999; Millour et al., 2018) to provide additional context for EXI observations.

The methodology follows Wang and Richardson (2015), M. Battalio and Wang (2019), and Gebhardt et al. (2022, 2023) and references therein. We used the Red-Green-Blue (RGB) composite, 635 nm, and 320 nm images for the detection of dust storms. Notably, the 635 nm images cannot always clearly distinguish between dust and water ice. Thus, the water ice sensitive 320 nm images were inspected to add more confidence to the separation between dust and water-ice clouds (Gebhardt et al., 2022, 2023). Here, we used the optical contrast between dust storms and the background to define the storm boundaries (M. Battalio & Wang, 2019). The boundaries were traced manually in the images and given a unique identifier so that each storm can be tracked if it lasts for multiple hours or sols (following e.g., M. Battalio & Wang, 2019; Guzewich et al., 2015). Also, we refer to the "dust storm instance" as the phase of a dust storm seen in a single EXI image at a particular time instant. We have used the same identifier (ID) for multiple instances of the same dust storm event. In the case of small-scale events, it is assumed that if two storm instances are not visible in subsequent (∼3 hr apart in case of XOS1 images) EXI images then they are not the same storm; accordingly, we changed the storm ID. Sometimes, the merging of multiple dust storms (with varying IDs) into a regional storm may occur (as explained in Section 3). In such cases, we have used the ID of the first storm in that sequence after merging. Notably, a "dust storm sequence" is the simultaneous occurrence of smaller storms (Wang & Richardson, 2015). However, unlike M. Battalio and Wang (2019), we have not assigned any sequence ID (separately from the storm instance ID) to these types of events. Here, our focus is to characterize the seasonal, diurnal, and spatial distribution of all the storm instances in general, not the "dust storm sequences" or their variability. This paper mainly focuses on non-polar dust storms (polar cap-edge dust storms were excluded) during L_s 49–360° of MY36, covering a major portion of the EMM primary mission.

3. The Dust Storm Database

The dust storm boundaries extracted from the EXI images were used to derive their centroid, area, and local true solar time of appearance to be listed in the dust storm database (Appendix). Notably, the EXI file naming convention used in the Appendix is discussed in Section 6 of the EXI Data Product Guide, available through the EMM science data center website (https://sdc.emiratesmarsmission.ae/documentation). In the database, we categorize the storms as local, large-local, and regional based on the thresholds of size (1.6×10^6 km^2) and duration (3 sols; Cantor et al., 2001). In our sample, no global dust storm event is observed (MY 36). The area threshold separates local storms from large-local and regional storms. We categorized dust storms with areas similar to a regional event but suspected to have a shorter duration as large-local events. Most of these categories are associated with northern hemispheric frontal dust events (Figure 1b). Sometimes the local or large-local categories are actually an early phase of a regional dust event, and they were given the same number (or ID). However, a different storm ID is assigned to any event that appeared over a different location (having a distinct boundary and separate centroid) and later merged into the regional dust event.

In this study, we have excluded the polar cap edge dust storms from the database. The reason for not considering the cap-edge storms is mostly due to the observational limitations of EMM. The maximum possible sub-spacecraft latitude of EMM is ±25°, which precludes the frequent observation of the high-latitude cap edge storms. Therefore, we ignore the polar cap-edge storms in the first place to avoid such bias in the distribution observed, even though there are images containing cap-edge storms (e.g., the dust storm studied in Gebhardt et al., 2022). Overall, we cataloged a total of 98 dust storms, with 248 instances through the end of MY 36. Sometimes these instances occurred within the same Martian day, allowing for diurnal movement or evolution of the storms. We observed four regional and 13 large-local dust events during the study period. This work is not focused on understanding the physics and dynamics of any particular storm, but rather highlights the diurnal, spatial, and seasonal variability of all the storms listed in the database. This version of the database will also be updated based on the data availability and lifespan of EMM. The following sections will present the findings from our database compilation along with some comparisons with the MDAD (M. Battalio & Wang, 2021).
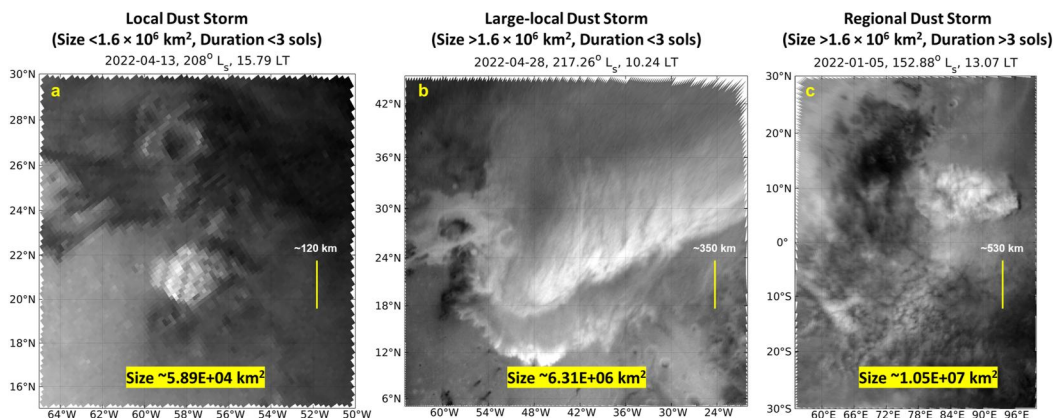
Figure 1. Dust storm categories based on their size and duration, showing the type of (a) local, (b) large-local, and (c) regional dust storm event. The images (at 635 nm) are map projected and extracted from level 2a of the EMM-EXI XOS1 observation set. The scaling is different in all the panels to illustrate the dust storms at varying spatial scales. Accordingly, a marker (yellow vertical line) is given to highlight the difference in scale. The local time (LT) is at the centroid longitude of the storm.

4. Results

4.1. Diurnal and Seasonal Variation of the Dust Storms

Figure 2a shows the diurnal distribution of the dust storm area derived from EXI images in 30° latitude bins considering all the storm instances during L_s 49–360° of MY36. Only one dust storm is present poleward of ±60°, as the polar cap-edge dust storms were not considered in this study. The number of storms for other latitude bins (between ±60°) is greater around the afternoon and lesser around the morning and evening hours, with their areas varying between 10^4 and 10^8 km^2 (Figure 2a). The highest number of occurrences are observed during late afternoon hours (around 14–16 hr local time), where the mid-latitude storms are more dominant (Figure 2b). There
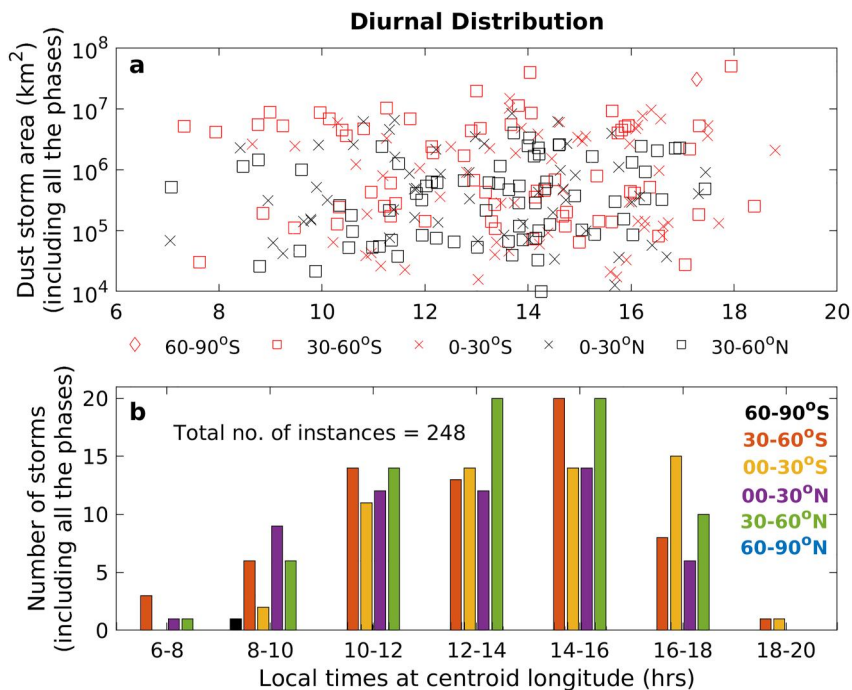

Figure 2. Diurnal distribution of the (a) dust storm area and (b) number of storms in different latitude bins during 6–20 hr local time, considering all the instances of these storms. The symbols in panel (a) indicate the latitudinal distribution of the dust storms.
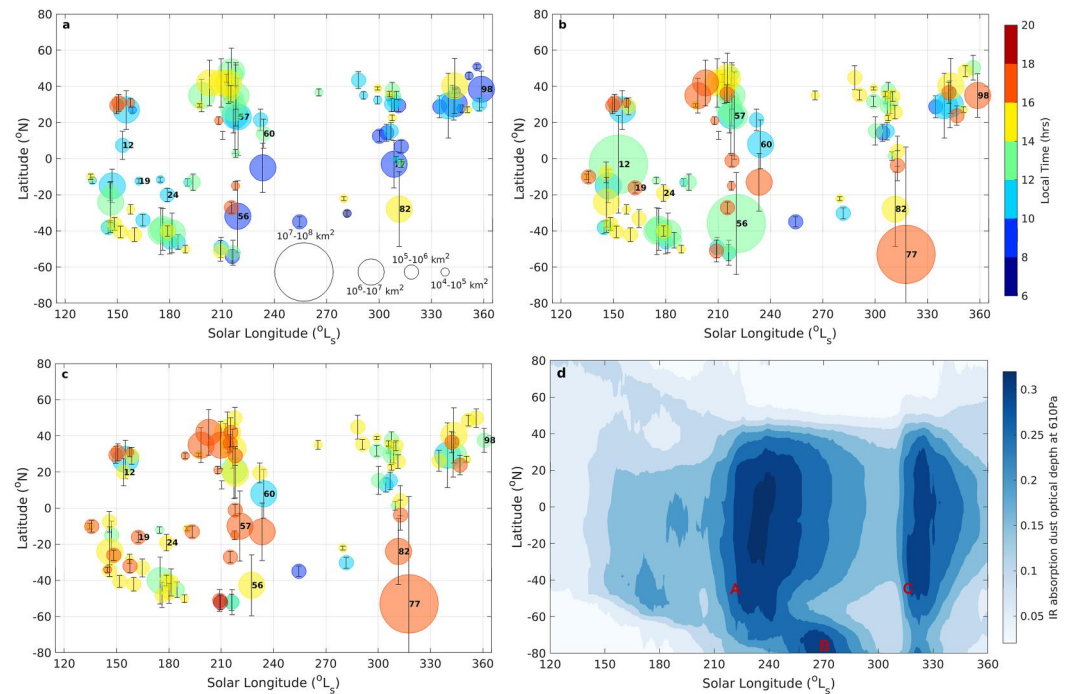
Figure 3. Seasonal and latitudinal distribution of dust storm area (circle area) with local times (shading) considering (a) initial phase, (b) peak phase, and (c) end phase for MY 36. The vertical bars represent the total latitudinal extent of the dust storm instances, and the unique storm identifiers are indicated by numbers. The seasonal distribution of column dust optical depth (in absorption at 9.3 microns) in the climatological year averaged over MYs 24–36 (but excluding periods with global dust storms in MY 25, 28, and 34) is also shown here in (d) for reference (Montabone et al., 2015, 2020). The conventional "A," "B," and "C" seasons for the dust storms are marked (Kass et al., 2016) in panel (d). The circle sizes are scaled by dust storm area with the legend in the bottom right of panel (a).

are only a few significant differences observed between 10 and 16 hr, such as southern mid-latitude storms peaking at 14–16 hr, while their northern counterparts peak at 12–16 hr. However, the difference between low- and mid-latitude storms in terms of the number of occurrences and area is not significant in most of the local time bins, except for 12–14 and 14–16 hr (Figure 2b). The atmospheric thermal tidal forcing is evident in the overall distribution of the storms at all low- and mid-latitude bins. The storms in the low latitudes and northern mid-latitudes follow the pattern of migrating diurnal tides with maxima in the early afternoon. In contrast, the semidiurnal component is more evident for dust storm occurrences over southern mid-latitudes (Barnes et al., 2017; Forbes et al., 2020). At these latitudes, the storm occurrences peak around 14–16 hr, which coincides more with the peak of the semi-diurnal mode (Forbes et al., 2020; Guerlet et al., 2023). Considering the hemispheric differences, the occurrence of northern mid-latitude storms is greater than its southern counterpart only around noon, whereas the low-latitude storms differ noticeably between each hemisphere during morning (8–10 LT) and evening (16–18 LT) hours. These observations are consistent with the fact that the diurnal variability is mainly driven by surface heating and radiative and convective heat transfer from the surface into the atmosphere (Barnes et al., 2017; Forbes et al., 2020; Hinson & Wilson, 2023).

Figure 3 highlights the seasonal and latitudinal distributions of the dust storms with color-coded markers, indicating their sizes (on the order of 10^4–10^8 km^2), centroid latitude, and local time of occurrence. The vertical bars represent the total latitudinal extent of the dust storm instances, and the unique storm identifiers are indicated by numbers. Figure 3 presents only the data starting from L_s 120°. Notably, MY 36 was mostly quiet in terms of dust storm occurrence in the beginning (L_s 49–120°) of the EMM science phase. The quiet time between $L_s = 100°$ and 120° is caused by the data gap due to the combination of solar conjunction and the spacecraft entering safe mode (Wolff et al., 2022). Also, this time of year is part of the conventional "low-dust-loading season" (L_s 10–140°), where dust storm occurrences (except the polar cap edge or frontal storms) are significantly less frequent than during the "high-dust-loading season" (L_s 140–10°) (e.g., Forget & Montabone, 2017; Guha et al., 2021; L. J.

Martin & Zurek, 1993; Montabone et al., 2015, 2020; Wang & Richardson, 2015). Therefore, solar longitudes smaller than 120° are omitted.

A recent understanding of the seasonal variability of dust storms defines multiple pseudo-seasons ($\approx 60°L_s$) with varying trajectories and timings of dust storm sequences (Wang et al., 2023). Here, the seasonal variation shows four potential clusters (centered around L_s 150°, 210°, 310°, and 350°) in the dust storm distribution, with the "solsticial pause" evident between L_s 240° and 270° (e.g., Lee et al., 2018; Lewis et al., 2016; Mulholland et al., 2016; Toigo & Waugh, 2022), and a "secondary pause" around L_s 320°. The primary storm clusters between L_s 125° and 240° (Figure 3) describe some similarity with the variation observed in the third and fourth "pseudo-seasons" (L_s 135–245°) of Wang et al. (2023). During this period, the storms over southern low- and mid-latitudes seem to be more frequent, which changes to their northern counterparts after the "solsticial pause" (Figure 3). Although the "secondary pause" observed here is not prominent in the last "pseudo-season" for MY 29–33, the overall seasonal variation shows striking similarities with other years considered by Wang et al. (2023).

The small-scale dust storm episodes (multiple occurrences within a short, sub-seasonal time scale) are prominent over northern mid-latitudes (Figure 3a), though the majority of the regional events were seen in southern mid-latitudes (Figures 3b and 3c). The latitudinal distribution of the northern mid-latitude storms (around 20°–40° N) suggests their possible origination from the potential "storm zones," such as the Arcadia, Acidalia, and Utopia regions (M. Battalio & Wang, 2021; Wang & Richardson, 2015). In contrast, the origination regions are possibly Argyre-Solis-Valles Marineris (ASV) or Hellas for southern hemispheric storms (M. Battalio & Wang, 2019).

Figures 3a–3c also suggest that the diurnal distribution of the dust storms over different latitudes varies with "pseudo-seasons." During L_s 120–180° (third pseudo-season), dust storms are more frequent over the southern hemisphere (SH), peaking at 12–14 hr in low latitudes and 14–16 hr in mid-latitudes, similar to what was seen in Figure 2. During L_s 180–240° (fourth pseudo-season), the number of storms is similar in both hemispheres. A noticeable change in the hourly distribution of the SH storms is observed during this period, with the highest number of mid-latitude storms during 10–16 hr, and low-latitude storms during 16–18 hr. During this period, the northern hemisphere (NH) low-latitude storms peak at 12–16 hr, which is 14–16 hr for the mid-latitude storms. The NH storms become more frequent during L_s 300–360° (sixth pseudoseason). With the spring season approaching, we see almost no change in the northern low-latitude storms during 8–16 hr, and southern low-latitude storms during 10–18 hr. During this period, the northern mid-latitude storms become more frequent during 10–14 hr (centered around noon). These findings again highlight the influence of solar insolation with varying seasons on the diurnal distribution. However, the seasonal dependencies on the hourly distribution of the storms are hard to decouple as the occurrence of the storms is not comparable between the two hemispheres. Dust storms are more frequent over either SH (L_s 120–180°) or NH (L_s 300–240°) during two out of three pseudo seasons. Moreover, the local time of occurrence suggests that the storms are more frequent in their peak phase between the afternoon and evening hours in both hemispheres (Figure 3b).

On the other hand, Figures 3b and 3c show the presence of storms during the "A" and "C" seasons (Kass et al., 2016). The "B" season storms usually occur at the baroclinic zone in the vicinity of the southern polar cap/vortex (Kass et al., 2016), which is not considered in this work (discussed in Section 3). In Figure 3d, we have used the climatology calculated over MYs 24–36 (but excluding periods with global dust storms in MY 25, 28, and 34), as the focus here is on the seasonality of the dust storms, not the variation in any particular year. The seasonal variation shows one (number 12) regional storm (in the order of 10^7–10^8 km^2) before the conventional dust storm season (L_s 180–360°) starts, though it is within the high-dust-loading season indicated by Montabone et al. (2015). The key point to note by comparing Figures 3a–3c is the variation in centroid latitude, Ls, and local time of occurrence between the start and end phases of the storms at all spatial scales (e.g., numbers 19, 24, 60, 82, 98, etc.). The movements in the centroid are most prominent for the regional storms (numbers 12, 56, 57, and 77). The movement of smaller storms is mostly random (either equatorward or poleward) in nature, and no correlation is observed between storm movement and seasons. In contrast, the regional dust events show a southward movement aligned with the seasonal surface level return flow during the dust storm season. This return flow is associated with the primary mean meridional circulation (of the Hadley cell) or regional flow such as "Western Boundary Currents (WBC)" induced by strong topography in the low latitudes (Barnes et al., 2017; Cantor, 2007; Joshi et al., 1995; Wang & Richardson, 2015).
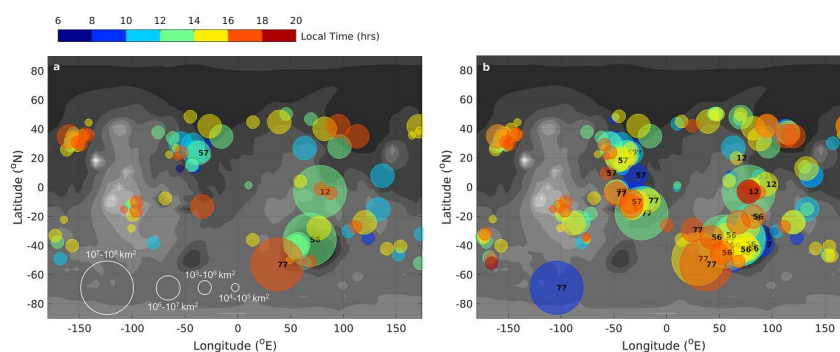
Figure 4. Spatial distribution of the dust storm area with local times considering their (a) peak phases and (b) all the phases for MY 36. Here, the topography is in the shaded grayscale contours and the circle sizes are scaled by dust storm area with the legend in the bottom left of the panel (a). Also, the unique identifiers for regional storms are indicated by numbers in both panels.

4.2. Diurnal and Spatial Distribution of the Dust Storms

Figure 4 illustrates the spatial distribution of all the storms observed by EXI during MY 36, with their local time of occurrence at centroid longitude and area. Figure 4a shows the distribution only at the peak phase of the storm, while Figure 4b considers all 248 instances of 98 dust storms of MY 36. The spatial distribution evidently indicates that the storms cluster near the major dust lifting regions (Wang & Richardson, 2015), such as Arcadia, Acidalia, and Utopia in the northern hemisphere and Cimmeria-Sirenum, Aonia-Solis-Valles Marineris, and Hellas regions in the southern hemisphere (Figure 4). These prominent mid-latitude storm clusters are connected through the so-called "corridors" (mostly centered around 50°E and 50°W), which are known for the dust storms' cross-equatorial movement (e.g., Cantor, 2007; Wang & Richardson, 2015). The main difference between Figures 4a and 4b is that the latter shows the Acidalia-Chryse and Utopia-Isidis corridors more clearly, whereas the Arcadia-Amazonis corridor is the same in both Figures 4a and 4b. Notably, these regions are situated in the vicinity of strong topography gradients that instigate the WBCs (Joshi et al., 1995). There is evidence for net dust lifting along the WBCs and net dust deposition between them (Gebhardt et al., 2020, 2021; Newman et al., 2005), which makes them a corridor for the cross-equatorial dust storm movement (Wang & Richardson, 2015). Overall, the number of northern hemispheric storms is greater because of frequent mid-latitude large-local storms (area mostly between 10^6 and 10^7 km^2). These storms can be attributed to the frontal activity caused by baroclinic instability, an example of which is shown in Figure 1b. The spatial distribution in Figure 4b is reminiscent of the dust storm distribution observed by Wang et al. (2023, their Figure 7) during the third and fourth "pseudo-seasons," consistent with a large number of storm occurrences in this period (Figure 3).

No significant difference in the preferred local time of occurrence for the peak phase of the dust storms is evident between the dust lifting regions mentioned above (Figure 4). The mid-latitude storms over the Arcadia-Amazonis region show a preferred local time for their peak phase around late afternoon (14–18 hr), whereas the storms (mostly frontal category) near the Acidalia and Utopia regions show their peak phase around 10–16 hr. The overall distribution suggests that peak phases of the storms are mostly preferred between 10 and 16 hr (Figure 4a), and they show a prominent movement of their centroid with local time evident in Figure 4b.

The spatial distribution of the dust storms shows a strong similarity with the distribution of surface albedo and thermal inertia (Cantor et al., 2001; Christensen et al., 2001). In Figure 4b, the regions with a large number of storms broadly correspond to high thermal inertia and low surface albedo. These high-inertia/dark surfaces are basically topographic lows having a potential for frequent dust storm generation. Notably, identifying the dust storm boundaries (or their detection to some extent) over bright surfaces may be challenging because of the sensitivity of the 635 nm band to both surface and dust features. However, a close comparison with the 320 nm band (UV) and RGB images helped to distinguish dust storm boundaries from bright surfaces whenever these were occasionally encountered. The surface wind stress (Figure 5) at 2 p.m. local time produced from the Mars Climate Database (MCD) is also consistent with the spatial distribution of the storms observed (Figure 4). 2-p.m. is chosen keeping in mind the greater number of storms (Figure 2), and their peak phases (Figure 4) around this time. Here, the surface wind stress is calculated from the MCD wind fields using the climatology average solar
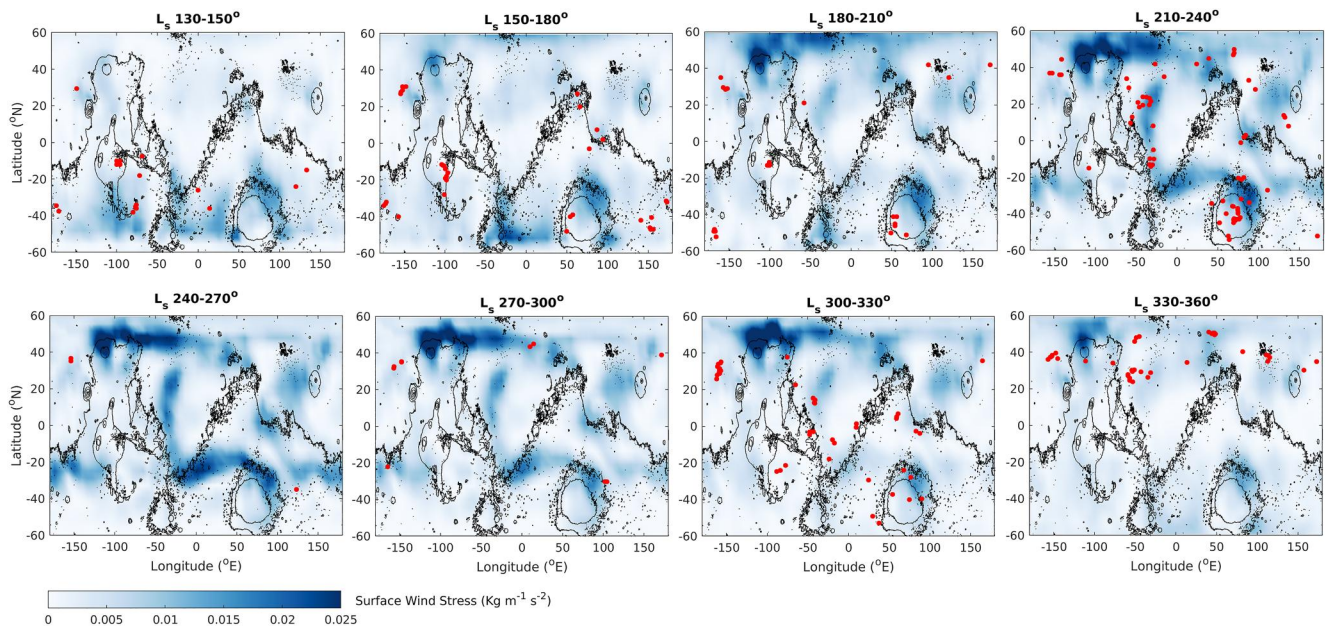
Figure 5. Seasonal variation of the surface wind stress at local time 2 p.m. (fixed at all longitudes) produced from the Mars Climate Database (v6.1) with climatology average solar scenario. The red dots represent the location of the dust storms during the 30° L_s period. Here, the first panel shows the storms between L_s 130° and 150°, similarly second panel is for storms between L_s 150° and 180°, and so on.

scenario. The wind stress is estimated using the methodology followed by Newman et al. (2002). Lifting by the surface wind stress is well known as one of the key mechanisms for dust loading into the atmosphere (e.g., Basu et al., 2004; Gebhardt et al., 2020; Newman et al., 2002). It is evident from Figure 5 that the surface wind stress is reasonably correlated with the spatial distribution of the storms, especially at L_s 240°, 270°, and 300° when the dust storm frequency is higher (Figures 3 and 4). The higher dust storm occurrences are visible over the Acidalia-Chryse and Utopia-Isidis corridors, and around 20–40°S (Figure 4b), where high wind stress can be observed (Figure 5). Previous modeling studies strongly suggest that wind stress lifting is responsible for most of the dust injection into the atmosphere during the dust storm season (Bagnold, 1954; Cantor et al., 2001; Haberle et al., 2003; Kahre et al., 2005; Newman et al., 2002, 2005). In contrast, the dust devil lifting mainly maintains the background dust haze during the low-dust season (Basu et al., 2004). Figure 5 shows a peak in wind stress during southern summer, especially over the regions of strong slope winds or thermal contrast flows (Newman et al., 2002), which is consistent with the observed storm clusters in Figure 4. However, there is high wind stress around 50°N and 50–100°W, which is consistent with low-level jets. In this case, the absence of correlation with the storm occurrences is due to not considering high-latitude storms, as can be seen in Figure 4. Therefore, the present findings are mostly consistent with previously published results (Kahre et al., 2005; Newman et al., 2002; Wang et al., 2023).

5. EMM Coverage Bias

The unique orbit of EMM enables it to have almost full local time and global coverage every 9–10 days (Figure 2 of Almatroushi et al. (2021)), which gives us an unprecedented observation at a sub-seasonal time scale. It is important to note that, unlike a sun-synchronous orbiter, one may not be able to observe daily changes all over the globe, as it takes around four EMM orbits (with ~55 hr orbital period) to fully cover the same. Therefore, it is relatively easy to overlook a local-scale dust storm event with a smaller area and shorter duration. This is not an issue for a regional or global dust storm event considering its average spatiotemporal scale, keeping in mind that even partial coverage of a regional storm can indicate a storm occurrence. Figure 6 shows the average percentage of pixels (excluding the pixels outside of the Martian disk) illuminated (in the EXI visible images) in each latitude bin at seven different local time bins. For example, 100% represents the full coverage, which means all pixels in that latitude and time bin are illuminated and seen by EXI. We can see that the EXI coverage on average varies between ~3 and 6% (±2%) for different latitude and local time
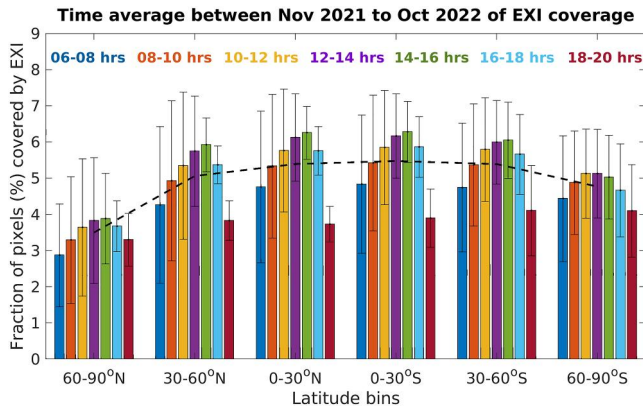
Figure 6. Local time (at seven bins starting from 6 to 20 hr) coverage of Emirates eXploration Imager at six latitude bins from November 2021 to October 2022. The black dashed line represents the average over all the local time bins. The vertical bars represent one standard deviation from the mean.

bins (Figure 6). The distribution of pixels covered by EXI is mostly symmetric between the northern and southern latitude bins, and the difference between the mean and 1σ deviation is not very large (Figure 6). This coverage range can be increased significantly if binned by $0.5°L_s$ or some more, for instance, $5°$ or $10°$ L_s (Figure not given). However, the latitudinal and local time distribution remains the same (e.g., distribution remains symmetric between northern and southern latitude bins) after $0.5°$ L_s binning. Also, the difference between different latitude bands is not significant (Figure 6), which suggests that the averaging time window has a systematic (not random) influence on EMM coverage. Therefore, it is possible to assess this systematic coverage bias.

In this context, we sampled the storm occurrences from MDAD based on the EXI coverage. MDAD is based on the global maps produced from 13 daily global wide-angle swaths taken around 3 p.m. local time by MARCI. Therefore, we binned the MDAD storms by $0.5°L_s$ for three Martian years and then sampled them based on the EXI coverage at an interval of $0.5°L_s$ (only between 14 and 16 hr local time). The aim here is to make the MDAD and EXI comparable taking into account their different time coverages before sampling of storm occurrence from MDAD based on the EXI coverage and to establish an empirical relation between the actual number of storms and the same modified by the EXI coverage. We have used the centroid latitude and longitude of each dust storm from MDAD and EXI f635 coverage information for this purpose. The dust storms from MDAD (during MY 29–31) were sampled for the same L_s of EXI observation (during MY 36). The sampled and actual storms were then binned into $5°$ latitude bins for a clear comparison. It is evident in Figures 7a–7c that the number of storms reduced by a factor of ~2 for all 3 years. The key point to note here is that in both cases there is no significant change in the overall latitudinal distribution, and it remains the same for all 3 years. This again indicates that the coverage bias is systematic and thus can be estimated using a polynomial fitting. The degree of polynomial fitting is chosen empirically without harming the precision of the solution; hence, the degree of polynomial is set to three (discussed in Text S1 of Supporting Information S1 and Figures S1–S2 of Supporting Information S2). We did not use the higher order (>third-degree) polynomial after reaching a reasonable solution while avoiding the overfitting problem. Here, the number of storms was arranged with latitude (at $1°$ intervals) before performing the polynomial fitting. $R^2 = 0.8$ (here, R is the correlation coefficient) confirms a strong correlation between the number of storms from MDAD and the same storms sampled by EXI coverage (Figure 7d).
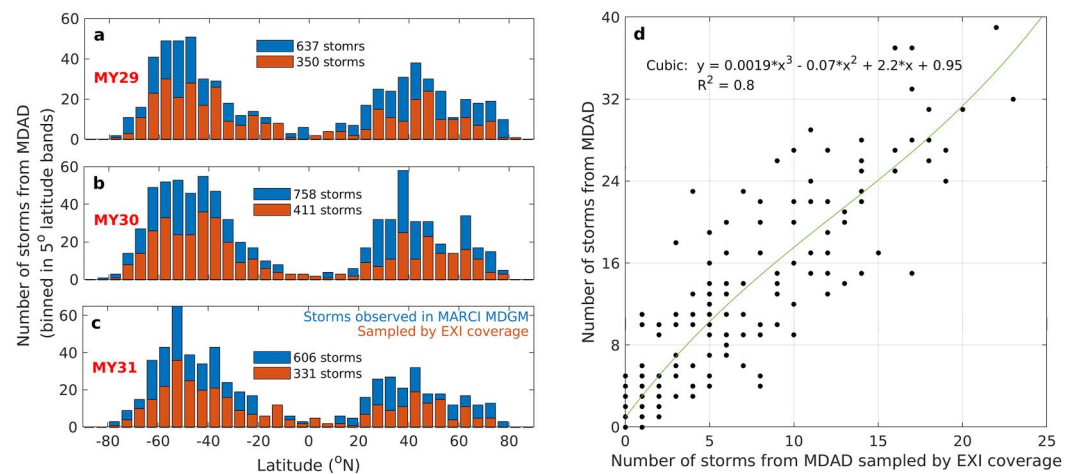

Figure 7. Dust storm distribution for (a–c) three Mars years (29–31) based on the Mars Dust Activity Database (M. Battalio & Wang, 2019) compared with the same but modified by the Emirates eXploration Imager coverage, and their empirical relation (d). In panels (a–c) the distribution shown by red bars is simulated/hypothetical, and is not the actual number. In panel (d), the number of storms is sampled by latitude and the fit is shown in green with the equation listed in the top left.
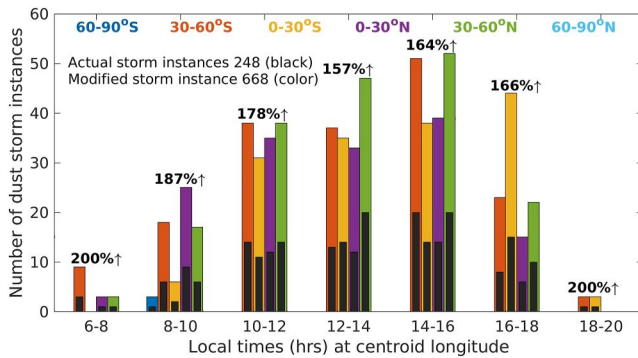
Figure 8. Latitudinal and local time distributions of the dust storm instances were modified based on the empirical relation established in Figure 7d. The increase percentage is also mentioned for each local time bin.

The present study then applied the empirical relation to the entire distribution of the storms from EXI. Notably, the empirical relation is based on the local times of 14–16 hr, but it has been applied to all the local times. This treatment is justified by similar coverage characteristics during 8–18 hr (no significant difference in coverage fraction in Figure 6), and a negligible number of storms outside this range (Figure 2b). It is worth mentioning that studying the diurnal variation is one of the key components of this work. That is why we applied the equation from Figure 7d to scale the EXI dust storm distribution (Figure 2b) for all the local time and latitude bins. Figure 8 illustrates the actual and modified latitudinal and local time distributions of the EXI dust storm instances. Figure 8 shows a more than two-fold increase (increasing to 668 from 248) in the total number of dust storms, but the local time distribution remains similar to what is observed in Figure 2b. The result highlights the nature of the EMM orbit and justifies EMM's observational findings on diurnal variation discussed in Section 4.

6. Summary

A comprehensive dust storm database has been compiled using images from the EXI aboard EMM. The primary focus was on tracking the spatial, sub-seasonal, and diurnal distribution of the surface area obscured by dust, a parameter estimated from either albedo contrast or Top of Atmosphere reflectance in relation to the surrounding terrain. The database includes essential details such as storm centroids, sizes, and local occurrence times, with a categorization based on storm size and duration. The systematic storm numbering in the database represents individual dust lifting events, allowing for effective tracking and analysis. Up to the end of Mars year 36, a total of 98 dust storms, comprising 248 instances, were cataloged, with an exclusion of polar cap edge dust storms. This database will continue to be updated as the mission progresses.

Among the observed dust storm events, several large-local storms (~10^6 km^2 but with smaller temporal extent) were predominantly observed over previously identified potential storm zones (Wang & Richardson, 2015), while four regional dust events were also identified. The diurnal distribution of the storms closely follows the diurnal thermotidal pattern. Northern hemisphere (NH) mid-latitude storms exhibit greater occurrence rates than southern hemisphere (SH) storms, primarily around noon. Additionally, low-latitude storms show noticeable differences between the hemispheres during morning and evening hours. Seasonal and latitudinal variations in the distribution of dust storms revealed four distinct clusters around Solar Longitude (L_s) 150°, 210°, 310°, and 350°. Notably, a "solstitial pause" was evident between L_s 240° and 270°, with a "secondary pause" around L_s 320°. The findings are reminiscent of previously observed sub-seasonal variations (Wang et al., 2023). Spatial analysis indicates a greater number of storms over the NH, particularly featuring more frequent mid-latitude large-local storms (area primarily between 10^6–10^7 km^2). Peak phases for the large storms mostly occur between 10 and 16 hr, displaying a pronounced movement of their centroids with local time. We observed no significant difference in the preferred local time of occurrence for the peak phase of the dust storms between different potential "storm zones." Surface wind stress exhibits a reasonable correlation with the spatial distribution of the storms, particularly at L_s 240°, 270°, and 300°, aligning with previous findings related to wind stress lifting (e.g., Newman et al., 2002).

EMM has almost full local time coverage but at a sub-seasonal time scale, which restricts a daily global observation, unlike any sun-synchronous orbiter. Therefore, an analysis of the influence of EXI coverage on observed dust storm distribution was conducted. EXI coverage varies between approximately 3%–6% for latitude and time bins when considering instantaneous image frames. The distribution appears mostly symmetric between the NH and SH latitude bands. When binned by 0.5°L_s or more, the coverage percentage increased significantly, while the overall distribution remained relatively unchanged. A systematic approach was employed to sample storm occurrences from the Mars Dust Activity Database (MDAD; M. Battalio & Wang, 2021) based on the EXI coverage bias, leading to the establishment of an empirical relationship between the actual number of storms and the modification introduced by EXI coverage. This approach resulted in a more than two-fold increase in recorded dust storm counts, with no significant change in the distribution pattern, highlighting the importance of accounting for coverage biases and justifying the observational findings of the present work.

Data Availability Statement

All the EXI images used here are publicly available at the EMM Science Data Center website (https://sdc.emiratesmarsmission.ae/data). The dust storm database related to this article can be found on the Zenodo online open-access repository (Guha, 2023). Column dust optical depth daily maps (Montabone et al., 2015, 2020) for MY 24 to 36 are publicly available on the Mars Climate Database (Forget et al., 1999; Millour et al., 2018) project webpage (https://www-mars.lmd.jussieu.fr/mars/info_web/index.html) at https://www-mars.lmd.jussieu.fr/mars/dust_climatology/index.html (NetCDF format) as well as on the Virtual European Solar and Planetary Access (VESPA) repository at https://vespa.obspm.fr (FITS format). The Mars Dust Activity Database used here can be accessed through the Zenodo online open access repository (J. M. Battalio et al., 2022).

References

Almatroushi, H., AlMazmi, H., AlMheiri, N., AlShamsi, M., AlTunaiji, E., Badri, K., et al. (2021). Emirates Mars mission characterization of Mars atmosphere dynamics and processes. *Space Science Reviews*, *217*(8), 89. https://doi.org/10.1007/s11214-021-00851-6

Amiri, H. E. S., Brain, D., Sharaf, O., Withnell, P., McGrath, M., Alloghani, M., et al. (2022). The Emirates Mars Mission. *Space Science Reviews*, *218*(1), 4. https://doi.org/10.1007/s11214-021-00868-x

Aoki, S., Vandaele, A. C., Daerden, F., Villanueva, G. L., Liuzzi, G., Thomas, I. R., et al. (2019). Water vapor vertical profiles on Mars in dust storms observed by TGO/NOMAD. *Journal of Geophysical Research: Planets*, *124*(12), 3482–3497. https://doi.org/10.1029/2019je006109

Bagnold, R. A. (1954). *The physics of blown sand and desert dunes*. Methuen.

Balme, M., & Greeley, R. (2006). Dust devils on Earth and Mars. *Reviews of Geophysics*, *44*(3). https://doi.org/10.1029/2005rg000188

Barnes, J. R., Haberle, R. M., Wilson, R. J., Lewis, S., Murphy, J. R., & Read, P. L. (2017). The global circulation. In R. M. Haberle, C. R. Todd, F. Forget, M. D. Smith, & R. W. Zurek (Eds.), *The Atmosphere and Climate of Mars. Cambridge Planetary Science* (pp. 229–294). Cambridge University Press.

Basu, S., Richardson, M. I., & Wilson, R. J. (2004). Simulation of the Martian dust cycle with the GFDL Mars GCM. *Journal of Geophysical Research*, *109*(E11), E11006. https://doi.org/10.1029/2004je002243

Battalio, J. M., Wang, H., Richardson, M., Toigo, A., & Saidel, M. (2022). Mars dust activity database (1.1) [Dataset]. *Zenodo*. https://doi.org/10.5281/zenodo.7480334

Battalio, M., & Wang, H. (2019). The Aonia-Solis-Valles dust storm track in the southern hemisphere of Mars. *Icarus*, *321*, 367–378. https://doi.org/10.1016/j.icarus.2018.10.026

Battalio, M., & Wang, H. (2021). The Mars Dust Activity Database (MDAD): A comprehensive statistical study of dust storm sequences. *Icarus*, *354*, 114059. https://doi.org/10.1016/j.icarus.2020.114059

Cantor, B. A. (2007). MOC observations of the 2001 Mars planet-encircling dust storm. *Icarus*, *186*(1), 60–96. https://doi.org/10.1016/j.icarus.2006.08.019

Cantor, B. A., James, P. B., Caplinger, M., & Wolff, M. J. (2001). Martian dust storms: 1999 Mars Orbiter Camera observations. *Journal of Geophysical Research*, *106*(E10), 23653–23687. https://doi.org/10.1029/2000je001310

Christensen, P. R., Bandfield, J. L., Hamilton, V. E., Ruff, S. W., Kieffer, H. H., Titus, T. N., et al. (2001). Mars Global Surveyor Thermal Emission Spectrometer experiment: Investigation description and surface science results. *Journal of Geophysical Research*, *106*(E10), 23823–23871. https://doi.org/10.1029/2000je001370

Clancy, R. T., Grossman, A. W., Wolff, M. J., James, P. B., Rudy, D. J., Billawala, Y. N., et al. (1996). Water vapor saturation at low altitudes around Mars aphelion: A key to Mars climate? *Icarus*, *122*(1), 36–62. https://doi.org/10.1006/icar.1996.0108

Fang, X., Ma, Y., Lee, Y., Bougher, S., Liu, G., Benna, M., et al. (2020). Mars dust storm effects in the ionosphere and magnetosphere and implications for atmospheric carbon loss. *Journal of Geophysical Research: Space Physics*, *125*(3), e2019JA026838. https://doi.org/10.1029/2019ja026838

Forbes, J. M., Zhang, X., Forget, F., Millour, E., & Kleinböhl, A. (2020). Solar tides in the middle and upper atmosphere of Mars. *Journal of Geophysical Research: Space Physics*, *125*(9), e2020JA028140. https://doi.org/10.1029/2020ja028140

Forget, F., Hourdin, F., Fournier, R., Hourdin, C., Talagrand, O., Collins, M., et al. (1999). Improved general circulation models of the Martian atmosphere from the surface to above 80 km. *Journal of Geophysical Research*, *104*(E10), 24155–24175. https://doi.org/10.1029/1999je001025

Forget, F., & Montabone, L. (2017). Atmospheric dust on Mars: A review. In *47th International Conference on Environmental Systems*.

Gebhardt, C., Abuelgasim, A., Fonseca, R. M., Martín-Torres, J., & Zorzano, M. P. (2020). Fully interactive and refined resolution simulations of the Martian dust cycle by the MarsWRF model. *Journal of Geophysical Research: Planets*, *125*(9), e2019JE006253. https://doi.org/10.1029/2019je006253

Gebhardt, C., Abuelgasim, A., Fonseca, R. M., Martín-Torres, J., & Zorzano, M. P. (2021). Characterizing dust-radiation feedback and refining the horizontal resolution of the MarsWRF model down to 0.5 degree. *Journal of Geophysical Research: Planets*, *126*(3), e2020JE006672. https://doi.org/10.1029/2020je006672

Gebhardt, C., Guha, B. K., Young, R. M. B., & Wolff, M. J. (2022). A frontal dust storm in the Northern Hemisphere at solar longitude 97—An unusual observation by the Emirates Mars mission. *Geophysical Research Letters*, *49*(20), e2022GL099528. https://doi.org/10.1029/2022gl099528

Gebhardt, C., Guha, B. K., Young, R. M. B., Wolff, M. J., & Edwards, C. S. (2023). Sub-hourly observations of dust storm growth, Lee waves, and Lyot crater, by the EMM camera EXI. *Geophysical Research Letters*, *50*(24), e2023GL105317. https://doi.org/10.1029/2023gl105317

Gillespie, H. E., Greybush, S. J., & Wilson, R. J. (2020). An investigation of the encirclement of Mars by dust in the 2018 global dust storm using EMARS. *Journal of Geophysical Research: Planets*, *125*(7), e2019JE006106. https://doi.org/10.1029/2019je006106

Guerlet, S., Fan, S., Forget, F., Ignatiev, N., Millour, E., Kleinböhl, A., et al. (2023). Thermal tides on Mars before and during the 2018 global dust event as observed by TIRVIM-ACS Onboard ExoMars Trace Gas Orbiter. *Journal of Geophysical Research: Planets*, *128*(9), e2023JE007851. https://doi.org/10.1029/2023je007851

Guha, B. K. (2023). Supporting data set for "Seasonal and diurnal variations of dust storms in Martian year 36 based on the EMM-EXI database" (Version 0) [Dataset]. *Zenodo*. https://doi.org/10.5281/zenodo.10275974

Guha, B. K., & Panda, J. (2021). Mixing time scales of dustiness and some associated effects at middle atmosphere during the 2018 global dust storm. *Advances in Space Research*, *68*(7), 3037–3051. https://doi.org/10.1016/j.asr.2021.05.030

Guha, B. K., & Panda, J. (2022). Analyzing vertical dust distribution and associated meteorological characteristics over Acidalia Planitia during a regional and global dust event. *Icarus*, *388*, 115230. https://doi.org/10.1016/j.icarus.2022.115230

Guha, B. K., Panda, J., & Chauhan, P. (2019). Analysing some martian atmospheric characteristics associated with a dust storm over the Lunae Planum region during October 2014. *Icarus*, *319*, 293–307. https://doi.org/10.1016/j.icarus.2018.09.018

Guha, B. K., Panda, J., Newman, C. E., & Richardson, M. I. (2021). Dust and water ice variability and their interaction pattern during Martian low-dust and high-dust periods. *Planetary and Space Science*, *209*, 105357. https://doi.org/10.1016/j.pss.2021.105357

Guzewich, S. D., Fedorova, A. A., Kahre, M. A., & Toigo, A. D. (2020). Studies of the 2018/Mars Year 34 planet-encircling dust storm. *Journal of Geophysical Research: Planets*, *125*(12), e2020JE006700. https://doi.org/10.1029/2020je006700

Guzewich, S. D., Lemmon, M., Smith, C. L., Martínez, G., de Vicente-Retortillo, Á., Newman, C. E., et al. (2019). Mars Science Laboratory observations of the 2018/Mars year 34 global dust storm. *Geophysical Research Letters*, *46*(1), 71–79. https://doi.org/10.1029/2018gl080839

Guzewich, S. D., Toigo, A. D., Kulowski, L., & Wang, H. (2015). Mars Orbiter Camera climatology of textured dust storms. *Icarus*, *258*, 1–13. https://doi.org/10.1016/j.icarus.2015.06.023

Haberle, R. M., Hollingsworth, J. L., Colaprete, A., Bridger, A. F. C., McKay, C. P., Murphy, J. R., et al. (2003). The NASA/AMES Mars general circulation model: Model improvements and comparison with observations. In *Mars atmosphere modeling and observations Workshop*.

Haberle, R. M., Leovy, C. B., & Pollack, J. B. (1982). Some effects of global dust storms on the atmospheric circulation of Mars. *Icarus*, *50*(2–3), 322–367. https://doi.org/10.1016/0019-1035(82)90129-4

Heavens, N. G., Kleinböhl, A., Chaffin, M. S., Halekas, J. S., Kass, D. M., Hayne, P. O., et al. (2018). Hydrogen escape from Mars enhanced by deep convection in dust storms. *Nature Astronomy*, *2*(2), 126–132. https://doi.org/10.1038/s41550-017-0353-4

Hinson, D., & Wilson, J. (2023). Diurnal waves forced by horizontal convergence of near-surface winds on Mars. *Icarus*, *394*, 115420. https://doi.org/10.1016/j.icarus.2022.115420

Jones, A. R., Wolff, M., Alshamsi, M., Osterloo, M., Bay, P., Brennan, N., et al. (2021). The Emirates Exploration Imager (EXI) instrument on the Emirates Mars Mission (EMM) Hope mission. *Space Science Reviews*, *217*(8), 1–56. https://doi.org/10.1007/s11214-021-00852-5

Joshi, M. M., Lewis, S. R., Read, P. L., & Catling, D. C. (1995). Western boundary currents in the Martian atmosphere: Numerical simulations and observational evidence. *Journal of Geophysical Research*, *100*(E3), 5485–5500. https://doi.org/10.1029/94je02716

Kahre, M. A., Murphy, J. R., Haberle, R. M., Montmessin, F., & Schaeffer, J. (2005). Simulating the Martian dust cycle with a finite surface dust reservoir. *Geophysical Research Letters*, *32*(20), L20204. https://doi.org/10.1029/2005gl023495

Kass, D. M., Kleinböhl, A., McCleese, D. J., Schofield, J. T., & Smith, M. D. (2016). Interannual similarity in the Martian atmosphere during the dust storm season. *Geophysical Research Letters*, *43*(12), 6111–6118. https://doi.org/10.1002/2016gl068978

Kass, D. M., Schofield, J. T., Kleinböhl, A., McCleese, D. J., Heavens, N. G., Shirley, J. H., & Steele, L. J. (2019). Mars Climate Sounder observation of Mars' 2018 global dust storm. *Geophysical Research Letters*, *47*(23), e2019GL083931. https://doi.org/10.1029/2019gl083931

Lee, C., Lawson, W. G., Richardson, M. I., Heavens, N. G., Kleinböhl, A., Banfield, D., et al. (2009). Thermal tides in the Martian middle atmosphere as seen by the Mars Climate Sounder. *Journal of Geophysical Research*, *114*(E3), E03005. https://doi.org/10.1029/2008je003285

Lee, C., Richardson, M. I., Newman, C. E., & Mischna, M. A. (2018). The sensitivity of solsticial pauses to atmospheric ice and dust in the MarsWRF General Circulation Model. *Icarus*, *311*, 23–34. https://doi.org/10.1016/j.icarus.2018.03.019

Lewis, S. R., Mulholland, D. P., Read, P. L., Montabone, L., Wilson, R. J., & Smith, M. D. (2016). The solsticial pause on Mars: 1. A planetary wave reanalysis. *Icarus*, *264*, 456–464. https://doi.org/10.1016/j.icarus.2015.08.039

Liu, J., Richardson, M. I., & Wilson, R. J. (2003). An assessment of the global, seasonal, and interannual spacecraft record of Martian climate in the thermal infrared. *Journal of Geophysical Research*, *108*(E8), 5089. https://doi.org/10.1029/2002je001921

Madeleine, J. B., Forget, F., Millour, E., Navarro, T., & Spiga, A. (2012). The influence of radiatively active water ice clouds on the Martian climate. *Geophysical Research Letters*, *39*(23), L23202. https://doi.org/10.1029/2012gl053564

Malin, M. C., Calvin, W. M., Cantor, B. A., Clancy, R. T., Haberle, R. M., James, P. B., et al. (2008). Climate, weather, and north polar observations from the Mars Reconnaissance Orbiter Mars Color Imager. *Icarus*, *194*(2), 501–512. https://doi.org/10.1016/j.icarus.2007.10.016

Martin, L. J., & Zurek, R. W. (1993). An analysis of the history of dust activity on Mars. *Journal of Geophysical Research*, *98*(E2), 3221–3246. https://doi.org/10.1029/92je02937

Martin, T. Z., & Kieffer, H. H. (1979). Thermal infrared properties of the Martian atmosphere: 2. The 15-µm band measurements. *Journal of Geophysical Research*, *84*(B6), 2843–2852. https://doi.org/10.1029/jb084ib06p02843

Medvedev, A. S., Yiğit, E., Hartogh, P., & Becker, E. (2011). Influence of gravity waves on the Martian atmosphere: General circulation modeling. *Journal of Geophysical Research*, *116*(E10), E10004. https://doi.org/10.1029/2011je003848

Millour, E., Forget, F., Spiga, A., Vals, M., Zakharov, V., Montabone, L., et al. (2018). The Mars climate database (version 5.3). In *Scientific Workshop: From Mars Express to ExoMars (27–28 February 2018, ESAC Madrid, Spain)*.

Montabone, L., Forget, F., Millour, E., Wilson, R. J., Lewis, S. R., Cantor, B., et al. (2015). Eight-year climatology of dust optical depth on Mars. *Icarus*, *251*, 65–95. https://doi.org/10.1016/j.icarus.2014.12.034

Montabone, L., Spiga, A., Kass, D. M., Kleinböhl, A., Forget, F., & Millour, E. (2020). Martian year 34 column dust climatology from Mars climate sounder observations: Reconstructed maps and model simulations. *Journal of Geophysical Research: Planets*, *125*(8), e2019JE006111. https://doi.org/10.1029/2019JE006111

Montmessin, F., Forget, F., Rannou, P., Cabane, M., & Haberle, R. M. (2004). Origin and role of water ice clouds in the Martian water cycle as inferred from a general circulation model. *Journal of Geophysical Research*, *109*(E10), E10004. https://doi.org/10.1029/2004je002284

Mulholland, D. P., Lewis, S. R., Read, P. L., Madeleine, J. B., & Forget, F. (2016). The solsticial pause on Mars: 2 Modelling and investigation of causes. *Icarus*, *264*, 465–477. https://doi.org/10.1016/j.icarus.2015.08.038

Newman, C. E., Lewis, S. R., & Read, P. L. (2005). The atmospheric circulation and dust activity in different orbital epochs on Mars. *Icarus*, *174*(1), 135–160. https://doi.org/10.1016/j.icarus.2004.10.023

Newman, C. E., Lewis, S. R., Read, P. L., & Forget, F. (2002). Modeling the Martian dust cycle, 1. Representations of dust transport processes. *Journal of Geophysical Research*, *107*(E12), 6-1–6-18. https://doi.org/10.1029/2002je001910

Piqueux, S., Kleinböhl, A., Hayne, P. O., Kass, D. M., Schofield, J. T., & McCleese, D. J. (2015). Variability of the Martian seasonal CO_2 cap extent over eight Mars Years. *Icarus*, *251*, 164–180. https://doi.org/10.1016/j.icarus.2014.10.045

Rafkin, S. C., Maria, M. R. S., & Michaels, T. I. (2002). Simulation of the atmospheric thermal circulation of a martian volcano using a mesoscale numerical model. *Nature*, *419*(6908), 697–699. https://doi.org/10.1038/nature01114

Smith, M. D., Pearl, J. C., Conrath, B. J., & Christensen, P. R. (2001). Thermal Emission Spectrometer results: Mars atmospheric thermal structure and aerosol distribution. *Journal of Geophysical Research*, *106*(E10), 23929–23945. https://doi.org/10.1029/2000je001321

Spiga, A., & Lewis, S. R. (2010). Martian mesoscale and microscale wind variability of relevance for dust lifting. *Mars*, *5*, 146–158. https://doi.org/10.1555/mars.2010.0006

Thomas, P., & Gierasch, P. J. (1985). Dust devils on Mars. *Science*, *230*(4722), 175–177. https://doi.org/10.1126/science.230.4722.175

Toigo, A. D., Richardson, M. I., Wilson, R. J., Wang, H., & Ingersoll, A. P. (2002). A first look at dust lifting and dust storms near the south pole of Mars with a mesoscale model. *Journal of Geophysical Research*, *107*(E7), 4-1–4-13. https://doi.org/10.1029/2001je001592

Toigo, A. D., & Waugh, D. W. (2022). Connections between the Transient Polar Warming and Solstitial Pause on Mars. *The Planetary Science Journal*, *3*(9), 208. https://doi.org/10.3847/psj/ac8550

Viúdez-Moreiras, D., Newman, C. E., De la Torre, M., Martínez, G., Guzewich, S., Lemmon, M., et al. (2019). Effects of the MY34/2018 global dust storm as measured by MSL REMS in Gale crater. *Journal of Geophysical Research: Planets*, *124*(7), 1899–1912. https://doi.org/10.1029/2019je005985

Wang, H., & Ingersoll, A. P. (2002). Martian clouds observed by Mars global surveyor Mars orbiter camera. *Journal of Geophysical Research*, *107*(E10), 8-1–8-16. https://doi.org/10.1029/2001je001815

Wang, H., & Richardson, M. I. (2015). The origin, evolution, and trajectory of large dust storms on Mars during Mars years 24–30 (1999–2011). *Icarus*, *251*, 112–127. https://doi.org/10.1016/j.icarus.2013.10.033

Wang, H., Saidel, M., Richardson, M. I., Toigo, A. D., & Battalio, J. M. (2023). Martian dust storm distribution and annual cycle from Mars daily global map observations. *Icarus*, *394*, 115416. https://doi.org/10.1016/j.icarus.2022.115416

Wilson, R. J. (1997). A general circulation model simulation of the Martian polar warming. *Geophysical Research Letters*, *24*(2), 123–126. https://doi.org/10.1029/96gl03814

Wolff, M. J., Fernando, A., Smith, M. D., Forget, F., Millour, E., Atwood, S. A., et al. (2022). Diurnal variations in the aphelion cloud belt as observed by the Emirates Exploration Imager (EXI). *Geophysical Research Letters*, *49*(18), e2022GL100477. https://doi.org/10.1029/2022gl100477

Wolkenberg, P. A. U. L. I. N. A., Giuranna, M., Smith, M. D., Grassi, D., & Amoroso, M. (2020). Similarities and differences of global dust storms in MY 25, 28, and 34. *Journal of Geophysical Research: Planets*, *125*(3), e2019JE006104. https://doi.org/10.1029/2019je006104

Zurek, R. W., Barnes, J. R., Haberle, R. M., Pollack, J. B., Tillman, J. E., & Leovy, C. B. (1992). Dynamics of the atmosphere of Mars. *Mars* (pp. 835–933).

Zurek, R. W., & Martin, L. J. (1993). Interannual variability of planet-encircling dust storms on Mars. *Journal of Geophysical Research*, *98*(E2), 3247–3259. https://doi.org/10.1029/92je02936